DRAFT VERSION MARCH 21, 2013
Preprint typeset using LaTeX style emulateapj v. 5/2/11

arXiv:1303.4728v2 [astro-ph.CO] 20 Mar 2013

WMAP OBSERVATIONS OF PLANCK ESZ CLUSTERS

YIN-ZHE MA,[1,2] GARY HINSHAW,[1] DOUGLAS SCOTT,[1]

Draft version March 21, 2013

ABSTRACT

We examine the Sunyaev-Zeldovich effect in the 7-year *WMAP* data by cross-correlating it with the *Planck* Early-release Sunyaev-Zeldovich (ESZ) catalogue. Our analysis proceeds in two parts. We first perform a stacking analysis in which the filtered *WMAP* data are averaged at the locations of the 175 *Planck* clusters. We then perform a regression analysis to compare the mean amplitude of the SZ signal, Y_{500}, in the *WMAP* data to the corresponding amplitude in the *Planck* data. The aggregate *Planck* clusters are detected in the 7-year *WMAP* data with a signal to noise ratio of 16.3. In the regression analysis we find the that the SZ amplitude measurements agree to better than 25%: $a = 1.23 \pm 0.18$ for the fit $Y_{500}^{\rm WMAP} = aY_{500}^{\rm Planck}$.

Subject headings: cosmology: the cosmic microwave background — galaxies: clusters: general —cosmology: large scale structure of universe — cosmology: observations

1. INTRODUCTION

Clusters of galaxies are important objects for studying cosmology and large scale structure formation. In hot clusters, around 12% of their mass is in the form of a hot, ionized intra-cluster medium (ICM, McCarthy et al. 2007). The ICM can be studied using direct X-ray imaging and/or the Sunyaev-Zeldovich effect (SZ, Sunyaev & Zeldovich 1972, 1980). Observations of the latter have grown tremendously in recent years thanks to an array of powerful new instruments (Birkinshaw & Gull 1978; Birkinshaw 1999; Carlstrom et al. 2002).

The thermal SZ effect is a secondary anisotropy in the the cosmic microwave background (CMB) radiation, caused by CMB photons scattering off free electrons in the hot ICM through the inverse Compton effect. The effect boosts the photon's energy and thus distorts the CMB spectrum in the direction of a cluster, causing a temperature decrement on the low frequency side of the CMB peak (specifically, $\nu < 217$ GHz), and an increment at high frequencies.

The SZ effect is especially powerful for studying high-redshift galaxy clusters. Since the Compton y-parameter (the integral of the ICM pressure along the line-of-sight) does not diminish with distance, and since the CMB has a nearly uniform surface brightness, the SZ effect does not diminish with increasing redshift. This makes SZ surveys especially suitable for finding high redshift clusters (Planck Collaboration VIII 2011). These cluster samples can be used to constrain cosmological models (e.g., from the evolution of the mass function) and to probe the physics of structure formation (e.g., from cluster scaling relations and structural properties, Planck Collaboration VIII 2011). Many ongoing experiments are measuring the SZ effect; for instance, the South Pole Telescope (SPT, Carlstrom et al. 2011) and the Atacama Cosmology Telescope (ACT, Marriage et al. 2011) are each measuring tens to hundreds of clusters over a few hundred square degrees (Haiman, Mohr & Holder 2001; Weller, Battye & Kneissl 2002; Levine, Schulz, & White 2002; Majumdar & Mohr 2004; Douspis, Aghanim & Langer 2006; Shaw, Rudd & Nagai 2011).

With the mission to precisely measure CMB temperature and polarization anisotropy, the *Planck* satellite was successfully launched by the European Space Agency (ESA) on 14 May 2009 (Planck Collaboration 2005). *Planck* carries a scientific payload consisting of 74 detectors sensitive to frequencies between 25 and 1000 GHz. *Planck* scans the sky continuously with an angular resolution between about 30 arcmin (FWHM) at the lowest frequency to about 4 arcmin at the highest (Planck Collaboration VIII 2011). Its combination of frequency coverage, sensitivity, and angular resolution, enables it to measure the spatial anisotropy of the CMB with an accuracy set by fundamental astrophysical limits.

Performing an SZ cluster survey over the full sky was an important goal for *Planck* (Aghanim et al. 1997), and the Project produced its Early Release Compact Source Catalogue (ERCSC, Planck Collaboration VII 2011) in 2011. The ERCSC included a catalogue of 189 SZ clusters detected with high-reliability from the first ten months of the *Planck* survey (see Planck ERCSC website). The Project is ultimately expected to release a few thousand high-reliability SZ clusters (Planck Collaboration XII 2011).

The *WMAP* mission was launched by NASA on 30 June 2001 to map the CMB anisotropy over the full sky to multipole moment $l \sim 1000$ (angular resolution $\sim 0.2^\circ$). *WMAP* has precisely measured the cosmological parameters to unprecedented accuracy, but its angular resolution and frequency coverage (23 to 94 GHz) were not optimized for SZ detection. *WMAP* independently detected a dozen SZ clusters, all of which were well-known (Komatsu et al. 2011). It is therefore interesting and important to see if the SZ clusters detected by *Planck* are also detected in the 7-year *WMAP* data. That is the aim of this paper.

The plan of this paper is as follows: in Section 2, we review the main features of the SZ effect and discuss the universal pressure profile we use to model the ICM pressure. In Section 3, we review the *Planck* ESZ catalogue and the *WMAP* W-band data which forms the basis of our analysis. In Section 4, we present the matched filter we apply to the *WMAP* sky map and examine the filtered model profiles for a range of cluster parameters. We present our main results in Section 4.3, and some concluding remarks follow.

Throughout this paper, we adopt a fiducial flat ΛCDM cosmology with Hubble constant $H_0 = 70\ {\rm km\,s^{-1}Mpc^{-1}}$, and mat-

---

[1] Department of Physics and Astronomy, University of British Columbia, Vancouver, V6T 1Z1, BC Canada
[2] Canadian Institute for Theoretical Astrophysics, Toronto, Canada

ter density parameter $\Omega_{\rm m} = 0.3$. The Hubble parameter at redshift z is $H(z) = H_0 E(z)$, where $E^2(z) = \Omega_{\rm m}(1+z)^3 + \Omega_\Lambda$.

2. CLUSTER PRESSURE PROFILE

2.1. *SZ effect*

The thermal SZ effect is a secondary anisotropy in the the cosmic microwave background (CMB) radiation, caused by CMB photons scattering off free electrons in the hot ICM through the inverse Compton effect. The effect boosts the photon's energy and thus distorts the CMB spectrum, causing a temperature decrement on the low frequency side of the CMB peak (specifically, $\nu < 217$ GHz), and vice versa. The induced temperature anisotropy in the direction of a cluster is (Sunyaev & Zeldovich 1972; Birkinshaw 1999; Carlstrom et al. 2002)

$$\frac{\Delta T}{T} = \left[\eta \frac{e^\eta + 1}{e^\eta - 1} - 4\right] y \equiv g_\nu y, \tag{1}$$

where $g_\nu \equiv [\eta(e^\eta+1)/(e^\eta-1)] - 4$ captures the frequency dependence, and

$$\eta = \frac{h\nu}{k_{\rm B} T_{\rm CMB}} = 1.76 \left(\frac{\nu}{100\ {\rm GHz}}\right). \tag{2}$$

The dimensionless Comptonization parameter y depends on the electron temperature, $T_{\rm e}(\mathbf{r})$, and density, $n_{\rm e}(\mathbf{r})$, in the ICM

$$y = \int n_{\rm e}(\mathbf{r}) \sigma_{\rm T} \frac{k_{\rm B} T_{\rm e}(\mathbf{r})}{m_{\rm e} c^2}\, dl, \tag{3}$$

where $\sigma_{\rm T}$ is the Thomson cross section, $k_{\rm B}$ is the Boltzmann constant, $m_{\rm e}c^2$ is the electron rest mass and the integral is taken along the line of sight. Since y is positive, the sign of g_ν determines whether ΔT is an increment or decrement in the CMB temperature. With $T_{\rm CMB} = 2.725$ K, we have $g_\nu > 0$ for $\nu > 217$ GHz, and vice versa, and $g_\nu \to -2$ at low frequencies ($\eta \ll 1$).

It is convenient to define the integrated SZ signal as $Y \equiv \int y\, d\Omega$, where the integration is over the solid angle of the cluster. This is equivalent to a volume integral

$$Y = \frac{1}{D_{\rm A}^2} \frac{\sigma_{\rm T}}{m_{\rm e} c^2} \int P dV, \tag{4}$$

where $D_{\rm A}$ is the angular diameter distance to the system and $P = n_{\rm e} k T_{\rm e}$ the electron pressure (Planck Collaboration VIII 2011). In the following, we denote the integral performed over the sphere of radius ${R_{500}}^3$ ($5R_{500}$), as Y_{500} (Y_{5R500}). Note that Y has units of solid angle, typically arcmin^2.

2.2. *Universal profile*

In order to study the SZ effect in the *WMAP* data, we need a model for the pressure profile of the cluster gas, $P(\mathbf{r})$. Arnaud et al. (2010) studied ICM pressure profiles using a sample of 33 local ($z < 0.2$) clusters observed with *XMM-Newton*. The sample spans a mass range of $10^{14} {\rm M}_\odot < {\rm M}_{500} < 10^{15} {\rm M}_\odot$, where M_{500} is the mass enclosed within R_{500} (assumed to be spherically symmetric). The pressure profiles in their sample can be described by a universal profile that is scaled with mass- and redshift-dependent factors. The dispersion of the data about the scaled profile is less than 30% beyond $0.2R_{500}$ (Arnaud et al. 2010).

With $x \equiv r/R_{500}$, the form of the universal profile given by Arnaud et al. (2010) is

$$P(x) = 1.65 \times 10^{-3} E(z)^{\frac{8}{3}} \left[\frac{M_{500}}{3 \times 10^{14} M_\odot h_{70}^{-1}}\right]^{\frac{2}{3} + \alpha_p + \alpha_p'} \times \tilde{p}(x)\, h_{70}^2 \left[{\rm keV\ cm^{-3}}\right], \tag{5}$$

where $h_{70} = (h/0.7)$, $\alpha_p = 0.12$, and

$$\alpha_p' = 0.1 - (\alpha_p + 0.1) \frac{(x/0.5)^3}{1 + (x/0.5)^3}. \tag{6}$$

Here $\tilde{p}(x)$ is the generalized NFW model proposed by Nagai, Kravtsov & Vikhlinin (2007) (see also Arnaud et al. 2010)

$$\tilde{p}(x) = \frac{P_0}{(c_{500} x)^\gamma \left[1 + (c_{500} x)^\alpha\right]^{(\beta - \gamma)/\alpha}}, \tag{7}$$

where $P_0 = 8.403 h_{70}^{-3/2}$ is the overall magnitude of the pressure profile, and c_{500}, γ, α, and β determine the slope of the profile. By fitting this pressure template to the simulated profile, Arnaud et al. (2010) found the best parameters are $c_{500} = 1.177, \gamma = 0.3081, \beta = 1.051$, and $\alpha = 5.4905$.

The only parameter left undetermined in Eq. (5) is the mass parameter M_{500}, which is nearly degenerate with the overall pressure normalization term P_0 in Eq. (7). To illustrate this degeneracy, we plot in Fig. 1a the normalized pressure profiles, $P(x)/P(0)$, for several combinations of M_{500} and the cluster redshift, z. They show very similar normalized profiles.

The angular profile of the model SZ signal is obtained by projecting the 3-dimensional pressure profile $P(\mathbf{r})$ onto the plane of the sky and calculating the corresponding temperature profile. Following Komatsu et al. (2011), the projected profile, in keV cm^{-3}, is

$$P_{2d}(\theta) = \int_{-\sqrt{r_{\rm out}^2 - \theta^2 D_{\rm A}^2}}^{\sqrt{r_{\rm out}^2 - \theta^2 D_{\rm A}^2}} P\left(\sqrt{l^2 + \theta^2 D_{\rm A}^2}\right) dl, \tag{8}$$

where the $D_{\rm A}$ is the angular diameter distance to redshift z, and $r_{\rm out}$ is the truncated radius, which we take to be $r_{\rm out} = 6R_{500}$. Beyond this range, the projection is not very sensitive to $r_{\rm out}$ because the profile falls off rapidly.

Given the 2-dimensional pressure profile, the temperature profile is

$$\frac{\Delta T_{\rm SZ}(\theta)}{T} = g_\nu \frac{\sigma_{\rm T}}{m_{\rm e} c^2} P_{2{\rm d}}(\theta), \tag{9}$$

and the Comptonization parameter y (Eq. (3)) is

$$\begin{aligned} y(\theta) &= \frac{\sigma_{\rm T}}{m_{\rm e} c^2} P_{2{\rm d}}(\theta) \\ &= \left(8 \times 10^{-3}\right) \int_0^{\sqrt{(6\theta_{500})^2 - \theta^2}\,\tilde{D}_{\rm A}} dx \\ &\times P\left(\sqrt{\left(\frac{x}{\theta_{500} \tilde{D}_{\rm A}}\right)^2 + \left(\frac{\theta}{\theta_{500}}\right)^2}\right), \end{aligned} \tag{10}$$

where we have used $\theta \equiv r/D_{\rm A}$.

In Fig. 1b, we plot the normalized Comptonization profile, $y(\theta)/y(0)$ vs. θ/θ_{500}, for the same four cluster parameters as in Fig. 1a. Again, the normalized y profiles are very similar. Since we fit the normalization of the profile to the *WMAP* data, we are primarily concerned with the angular radius of

---

[3] R_{500} is defined as the radius within which the density contrast is > 500.

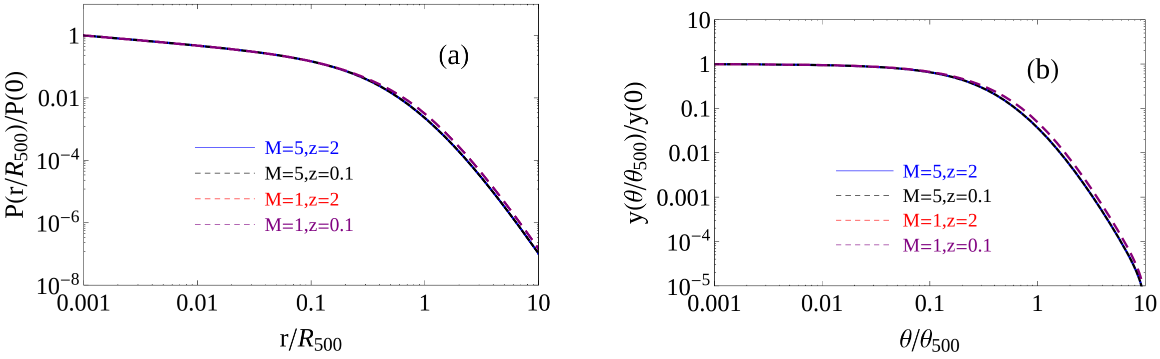

FIG. 1.— *Left* – Pressure profile from Eq. (5) for four hypothetical clusters. *Right* – The temperature profile from Eq. (10) for the same four cluster parameters. The units of M, R_{500}, and θ_{500} are $3\times10^{14}\mathrm{M}_\odot$, Mpc, and arcmin, respectively.

each cluster, θ_{500}, which scales the extent of the profile. As discussed below, this parameter may be derived from information provided in the *Planck* ESZ catalogue. Thus, when fitting the *WMAP* data, we adopt the normalized profile in Eq. (10) using the θ_{500} value predicted by *Planck*.

3. DATA DESCRIPTION

In this section, we introduce the data used in our analysis: the *Planck* Early SZ catalogue, which consists of 189 clusters; and the *WMAP* W-band sky map that will be used for consistency testing.

3.1. *Planck ESZ catalogue*

Planck is a full-sky CMB survey with nine different frequency channels: 30, 44, 70, 100, 143, 217, 353, 545, and 857 GHz. The FWHM angular resolution for these channels are 33, 24, 14, 10, 7.1, 5, 5 and 5 arcmin, respectively.

The ESZ catalogue was obtained from a blind, multi-frequency search of the *Planck*-HFI maps, using on an all-sky extension of the algorithm given in Melin et al. (2006). The team used a matched multi-frequency filter method to enhance signal-to-noise in the 189 detected objects; the filter optimizes detectability by using a linear combination of frequency maps to null the CMB signal, and spatial filtering to suppress foregrounds and instrument noise (Planck Collaboration VIII 2011). In principle, SZ clusters can be also seen in the three LFI channels; however, the low-frequency beam size (∼25 arcmin) is generally much larger than a typical cluster size of ∼5 arcmin, therefore the LFI channels were not included in the analysis (Planck Collaboration VIII 2011). The position and radius ($5R_{500}$) of each cluster profile was varied to maximize the signal-to-noise ratio of each detection. The position, angular radius, $5\theta_{500}$, and integrated Comptonization parameter, Y_{5R500}, are tabulated for each cluster in the catalogue (Planck Collaboration VIII 2011)[4].

Their preliminary analysis yielded 201 high signal-to-noise ($S/N > 6$) candidates, of which 189 were deemed to be of high reliability. Of these, 169 were already known from X-ray and optical surveys, while 20 clusters were newly detected. The new clusters were subsequently confirmed by *XMM-Newton* observations (Planck Collaboration IX 2011) and by the AMI survey (Zwart et al. 2008).

Redshifts are known for 175 of the 189 clusters. Since we require redshift information to construct a pressure profile, we limit our analysis of *WMAP* data to this subset of the full catalogue. The redshift distribution and positions of the *Planck* ESZ clusters are shown in Fig. 2: in the left panel *a*, the redshift distribution of these clusters is seen to range from 0.01 to 0.5 with a mean redshift of 0.18. They are distributed uniformly across the sky, outside a $|b| < 14^\circ$ galaxy cut.

3.2. *WMAP W-band data*

The *WMAP* satellite produced full-sky maps at five frequency bands from 23 to 94 GHz, with a FWHM angular resolution from 52.8 to 13.2 arcmin, respectively. These maps were used to measure cosmological parameters with unprecedented accuracy.

Taking into account the combined effects of spectral shape, g_ν, and diffraction-limited beam size, the largest SZ *decrement* occurs around 140 GHz (Carlstrom et al. 2002), which is higher than the highest *WMAP* frequency. Within the *WMAP* bands, the 94 GHz W-band map has the most sensitivity to SZ signal, owing mostly to its angular resolution (and relatively low foreground contamination). In the following analysis, we fit SZ profiles to the 7-year W-band sky map. At 94 GHz, the SZ decrement is $\Delta T_{\rm SZ}/T = -1.56y$.

4. FILTERING TECHNIQUE

To optimally characterize the SZ signal, we need to filter the observed maps, which are dominated by primary CMB fluctuations, but which also include residual foreground signals (including extragalactic point sources) and instrument noise. In this section we describe the choice of filter (Tegmark & de Oliveira-Costa 1998), calculate the temperature profile of SZ clusters after filtering, and compute the Y-parameter. We then compare Y_{500} derived from *WMAP* with that derived from *Planck*.

4.1. *Optimal filter*

SZ clusters are typically unresolved in the *WMAP* beam, so we treat them as the point sources on the sky. In this limit, if cluster i has flux S_i at sky position $\hat{r}_i$, the sky temperature $\Delta T(\hat{r})$ may be written as

$$\Delta T(\hat{r}) = c\sum_i S_i\delta(\hat{r},\hat{r}_i) + \sum_{\ell m} a_{\ell m}Y_{\ell m}(\hat{r}), \tag{11}$$

where δ is the Dirac delta function, and c is the conversion factor between flux and temperature, given by

$$c = c_*\frac{\left[2\sinh(\frac{\eta}{2})\right]^2}{\eta^4},\ c_* = \frac{1}{2k_{\rm B}}\left(\frac{hc}{kT_{\rm CMB}}\right)^2 \simeq \frac{10\ \rm mK}{\rm MJysr^{-1}}, \tag{12}$$

---

[4] With the assumption of spherical symmetry in the model profile, we have $Y_{5R500} = 1.8\times Y_{500}$.

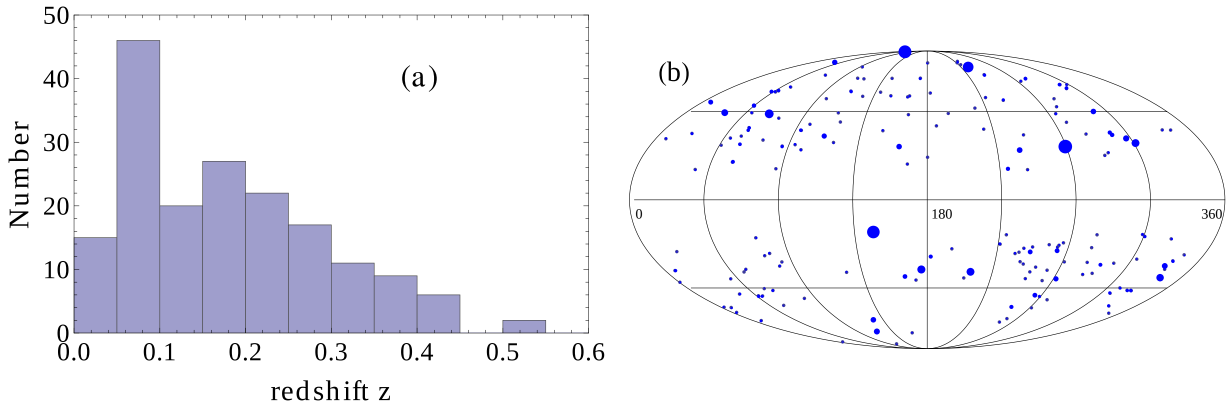

FIG. 2.— *Left* – the redshift histogram of 175 *Planck* ESZ clusters. *Right* – the full-sky distribution of *Planck* ESZ clusters; the size of each point is proportional to the angular radius θ_{500}.

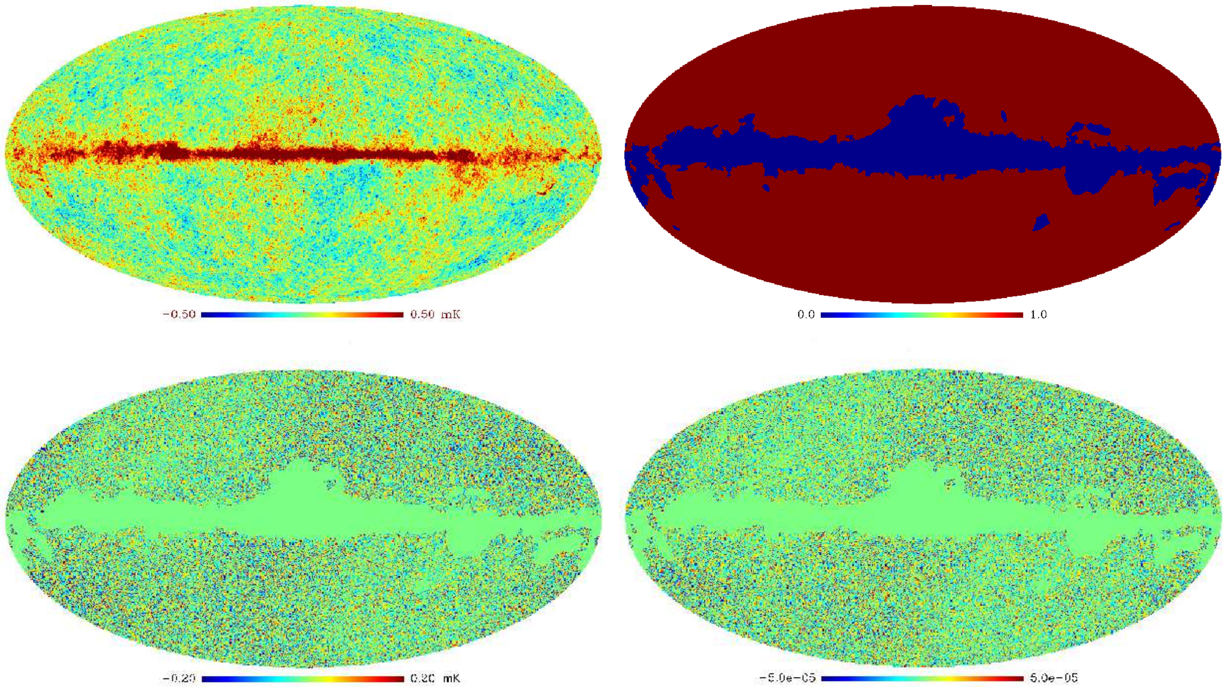

FIG. 3.— *WMAP* data used in this analysis. *Upper-left* – co-added 7-year W-band map. *Upper-right* – *WMAP* 7-year analysis mask, including point source cuts, 82.4% of the sky remains. *Lower-left* – the filtered W-band temperature map, as per Eq. (15). *Lower-right* – the dimensionless y-parameter map, as per Eq. (10).

where η is defined in Eq. (2) (see also Tegmark & Efstathiou 1996; Tegmark & de Oliveira-Costa 1998). Here, the spherical harmonic coefficients $a_{\ell m}$ characterize the true CMB temperature fluctuation. The sky signal convolved with the beam response, B_ℓ, is

$$\Delta T^{\rm obs}(\hat{r}) = c \sum_i S_i \left(\sum_\ell \frac{2\ell+1}{4\pi} P_\ell(\hat{r}\cdot\hat{r}_i) B_\ell \right) + \sum_{\ell m} a^{\rm tot}_{\ell m} Y_{\ell m}(\hat{r}), \tag{13}$$

where $a^{\rm tot}_{\ell m}$ encodes the temperature due to CMB fluctuations, convolved with the beam, and detector noise, not convolved with the beam,

$$a^{\rm tot}_{\ell m} = a^{\rm CMB}_{\ell m} B_\ell + n_{\ell m}, \tag{14}$$

where the beam transfer function, B_ℓ, is obtained from LAMBDA website. [Note: in this analysis, we use the foreground-cleaned maps supplied by the *WMAP* team, and impose the *WMAP* 7-yr analysis mask (Fig. 3b); we also neglect residual foreground signals in the cleaned, masked maps.] Fig. 4 compares the angular power spectrum, C_ℓ, directly estimated from the map with the spectrum predicted by Eq. (14) using the best-fit ΛCDM model. The predicted spectrum agrees with the measured spectrum very well.

To maximize our sensitivity to point sources, we further convolve the observed map $\Delta T^{\rm obs}$ with an optimal filter W_ℓ, so that

$$\Delta\tilde{T}(\hat{r}) = c \sum_i S_i \left(\sum_\ell \frac{2\ell+1}{4\pi} P_\ell(\hat{r}\cdot\hat{r}_i) B_\ell W_\ell \right)$$

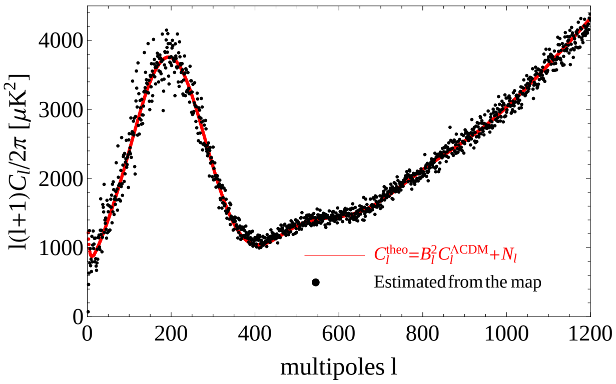

FIG. 4.— The measured (black) and predicted (red) power spectra, C_ℓ, from the *WMAP* 7-year W-band map. The predicted spectrum is based on the best-fit ΛCDM model convolved with the beam, plus detector noise, assuming $N_\ell \equiv 0.0187\ \mu{\rm K}^2$ (Hinshaw et al. 2007).

$$+\sum_{\ell m} a_{\ell m}^{\rm tot} W_\ell Y_{\ell m}(\hat{r}). \qquad (15)$$

Note that this form implicitly assumes that the beam response and optimal filter are both azimuthally symmetric. Treating the second line in Eq. (15) as the noise term, we seek the form of W_ℓ that maximizes the cluster signal to noise. In the direction of cluster i, the filtered signal is $\Delta\tilde{T}(\hat{r}_i) = AS_i$, where

$$A \equiv c \sum_\ell \frac{2\ell+1}{4\pi} B_\ell W_\ell = \text{constant}. \qquad (16)$$

We choose W_ℓ to minimize the ratio

$$\sigma^2 = {\rm Var}\left(\frac{\Delta\tilde{\rm T}}{\rm A}\right) = \frac{\sum_\ell \frac{2\ell+1}{4\pi} {\rm C}_\ell^{\rm tot} {\rm W}_\ell^2}{{\rm c}^2 \left(\sum_\ell \frac{2\ell+1}{4\pi} {\rm B}_\ell {\rm W}_\ell\right)^2}, \qquad (17)$$

where $C_\ell^{\rm tot} \equiv B_\ell^2 C_\ell^{\rm CMB} + N_\ell$, and we take $C_\ell^{\rm CMB}$ to be the ΛCDM model power spectrum.

We minimize Eq. (17) by adding a Lagrange multiplier to the numerator,

$$\sum_\ell \frac{2\ell+1}{4\pi} C_\ell^{\rm tot} W_\ell^2 + \lambda \left(\sum_\ell \frac{2\ell+1}{4\pi} B_\ell W_\ell\right)^2, \qquad (18)$$

and minimizing with respect W_ℓ. We obtain

$$W_\ell \sim \frac{B_\ell}{B_\ell^2 C_\ell^{\rm CMB} + N_\ell} = \frac{B_\ell}{C_\ell^{\rm tot}}. \qquad (19)$$

The normalization of W_ℓ does not affect the signal-to-noise ratio of the cluster detection. We plot W_ℓ in Fig. 5; note that W_ℓ is maximal in the range $\ell \sim 500-1000$. With this filter, the smallest variance we can obtain for point source is

$$\sigma^2 = c^{-2} \left(\sum_\ell \frac{2\ell+1}{4\pi} \frac{B_\ell^2}{C_\ell^{\rm tot}}\right)^{-1}. \qquad (20)$$

4.2. *The filtered cluster profile*

What is the shape of the universal cluster profile after filtering? Let the unfiltered temperature map due to N clusters at positions $\hat{r}_i$, $i = 1, \ldots, N$, be

$$x(\hat{r}) = \sum_i f_i(\Theta_i), \qquad (21)$$

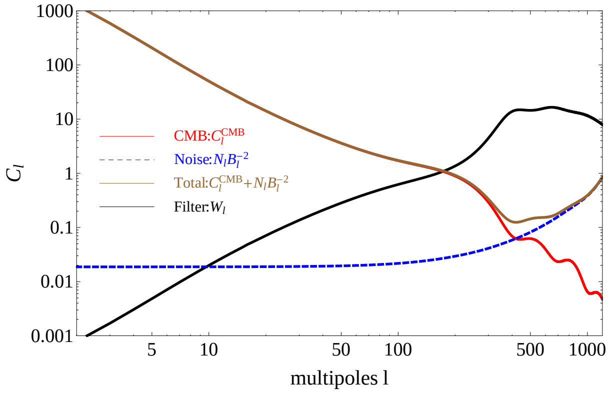

FIG. 5.— The optimal filter (black) for point source detection in the *WMAP* 7-year W-band map, Eq. (19). The CMB signal (red) and detector noise (blue) are shown for comparison.

where f_i is the profile of the ith cluster, and Θ_i is the angle between the ith cluster and $\hat{r}$,

$$\cos\Theta_i = \hat{r}_i \cdot \hat{r} = \cos\theta_i \cos\theta + \sin\theta_i \sin\theta \cos(\phi - \phi_i). \qquad (22)$$

The filtered cluster map may be written as

$$\begin{aligned} \tilde{x}(\hat{r}) &= (W * x)(\hat{r}) \\ &= \sum_i \left[\int d\Omega'\, f_i(\Theta') W(\cos\Theta')\right], \qquad (23) \end{aligned}$$

where

$$W(\cos\Theta') = \sum_\ell \frac{2\ell+1}{4\pi} W_\ell P_\ell(\cos\Theta'), \qquad (24)$$

and $\cos\Theta' = \hat{r} \cdot \hat{r}'$. In the limit that the SZ clusters can be considered point sources, $f_i(\Theta_i) = cS_i\delta(\hat{r}_i, \hat{r})$, the filtered map reduces to

$$\tilde{x}(\hat{r}) = c \sum_i S_i \sum_\ell \frac{2\ell+1}{4\pi} W_\ell P_\ell(\cos\Theta_i). \qquad (25)$$

In Fig. 6, we plot selected SZ cluster profiles before and after the filtering. For the small cluster case shown in Fig. 6a, the filtered profile does not differ appreciably from a filtered point source because the cluster is unresolved. For larger cluster (Fig. 6b), the filtered profile is noticeably different from a filtered point source profile. In either case, we note that θ_{500} lies within the radius where the filtered profile is still positive, so this filter should not suppress actual SZ signal. We consider this question in more detail in the following section.

4.3. *Results of filtering*

The filtered *WMAP* 7-year W-band map is shown in the lower-left panel of Fig. 3. This map exhibits suppression of CMB signal over a range of angular scales. The dimensionless y-map obtained from Eq. (10) is shown in the lower-right panel of Fig. 3. We calculate Y_{500} for each cluster and tabulate the results in column 8 of Tables 2–4. To evaluate the uncertainty in Y_{500}, we simulate 1000 sky maps with CMB signal and pixel noise. For each map we calculate Y_{500} at each cluster position, then compute the standard deviation over the ensemble of maps. The resulting error is given in column 9 of Tables 2–4.

Because of beam dilution and detector noise in the *WMAP* data, the signal-to-noise ratio for the detection of individual SZ clusters is relatively low; however, the stacked signal is

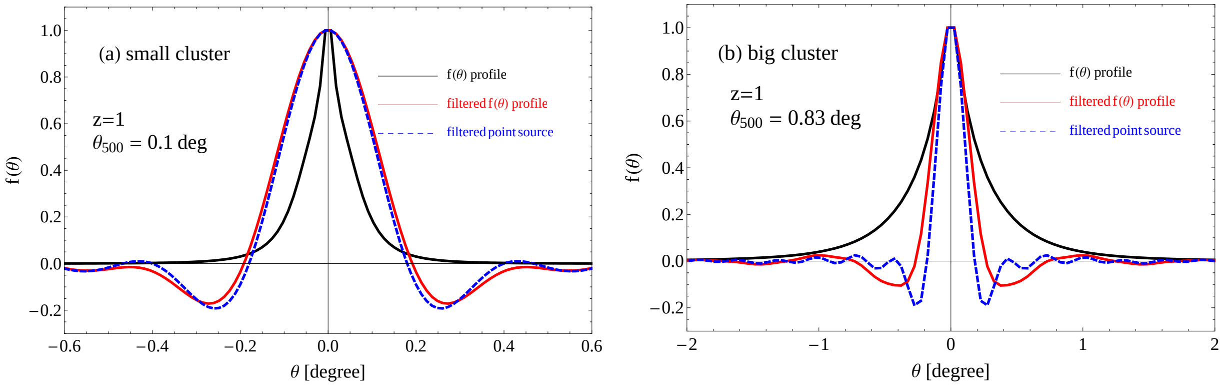

FIG. 6.— The shape of selected cluster profiles before and after filtering. Left - a small cluster with θ_{500} less than the *WMAP* W-band beam size, 0.22°; right - a marginally resolved cluster.

TABLE 1
AGGREGATE SIGNAL-TO-NOISE FOR STACKED SZ CLUSTERS

Method	*WMAP*	*Planck*
unweighted, Eq. (26)	8.9	85.2
weighted, Eq. (27)	16.3	123.3

significant. In Table 1 we give the aggregate signal-to-noise ratio for two methods of stacking: unweighted and weighted. In the first method we evaluate

$$\frac{\sum_i Y_i}{\left(\sum_i \delta Y_i^2\right)^{1/2}}, \tag{26}$$

which equally weights all cluster detections. The total signal-to-noise ratio for this method is 8.9 for *WMAP* and 85.2 for *Planck*. In the second method we evaluate

$$\left[\sum_i \left(\frac{Y_i}{\delta Y_i}\right)^2\right]^{1/2}, \tag{27}$$

which down-weights clusters with low signal-to-noise. This gives an aggregate signal-to-noise of 16.3 for *WMAP* and 123.3 for *Planck*. In Fig. 7 we show the aggregate SZ profile from the stacked *WMAP* data and compare this to the predicted profile based on stacking the universal pressure profile, scaled by the measured Comptonization parameters from the *Planck* catalogue.

Next, we assess the consistency between the *WMAP* and *Planck* cluster detections. Figure 8 compares the integrated Comptonization parameter, Y_{500}, from each data set. While there is quite a bit of scatter, the two measurements are clearly correlated. We use linear regression with errors in both axes to fit the slope between the two data sets (see Appendix A). Using Eq. (A5), we find

$$Y_{500}^{\rm wmap} = (1.23 \pm 0.18) \times Y_{500}^{\rm planck} \text{ (68\% CL)}, \tag{28}$$

which is within 2σ of unity. Fig. 8 shows the best-fit regression in red.

While the measured slope is perfectly consistent with unity, we briefly consider some potential sources of systematic error in our comparison. (1) The amplitude of $Y_{500}^{\rm wmap}$ depends on how one treats the monopole moment in the *WMAP* map. In our analysis, we subtract the monopole both before and after we apply the optimal filter to the map. (2) Finite pixel size can introduce noise when identifying pixels within an area that is not much larger than the pixel size. We account for this effect in our Monte Carlo evaluation of the $Y_{500}^{\rm wmap}$ uncertainty. (3) For clusters with θ_{500} larger than the *WMAP* W-band beam width of 0.21°, the integral for Y_{500} includes some negative regions in the filtered profile, as shown in Fig. 6. This will suppress the integrated signal in those clusters. The smaller value of $Y_{500}^{\rm wmap}$ measured in the COMA cluster, compared to $Y_{500}^{\rm planck}$, is due to this effect. We note that our value is consistent with that reported by Komatsu et al. (2011)[5]. (4) While the *Planck* team documented their detection of SZ clusters (Planck Collaboration VIII 2011; Planck Collaboration VII 2011; Planck Collaboration IX 2011), some processing details are not completely clear, such as the precise choice of filter. Despite these uncertainties, the best-fit slope between $Y_{500}^{\rm wmap}$ and $Y_{500}^{\rm planck}$ is consistent with unity and suggests that such effects are not significant.

5. CONCLUSION

The *Planck* collaboration released its ESZ cluster catalogue in Jan 2011. It contained 189 SZ clusters across the full sky, 175 of which had tabulated redshifts. In this paper, we examine these 175 cluster locations in the *WMAP* data to assess consistency with the *Planck* catalogue.

We assume the clusters are described by a universal pressure profile, Eq. (5), and project the 3-d profile onto the plane of the sky. Given this profile, we can calculate the integrated Comptonization parameter, Y_{500}, for any cluster location determined by *Planck*. We filter the *WMAP* 7-year W-band data with an optimal filter to suppress primary CMB signal and detector noise, then examine the effects of the filter on the universal pressure profile. We conclude that the angular radius, θ_{500}, adequately captures the bulk of the SZ signal in the filtered data. We estimate the uncertainty in Y_{500} using 1000 Monte Carlo realizations of a ΛCDM CMB signal and detector noise.

We perform two consistency tests between $Y_{500}^{\rm wmap}$ and $Y_{500}^{\rm planck}$. First, we stack all the cluster data to estimate the total signal-to-noise ratio. In the weighted stacking, we obtain an aggregate signal-to-noise ratio of 16.3 from the *WMAP* data, which clearly indicates that *WMAP* detects the most significant clusters seen by *Planck*.

[5] Komatsu et al. (2011) do not give an explicit value for Y_{500}, but from the measured dimensionless quantity $y \sim 7 \times 10^{-5}$ (two equations after Eq. (71)), and the profile width of $10.3'$ (three lines above Eq. (70) and figure 14), we estimate that their measured value of Y_{500} for COMA would be ~ 0.01 arcmin^2, which is consistent with our finding within the errors.

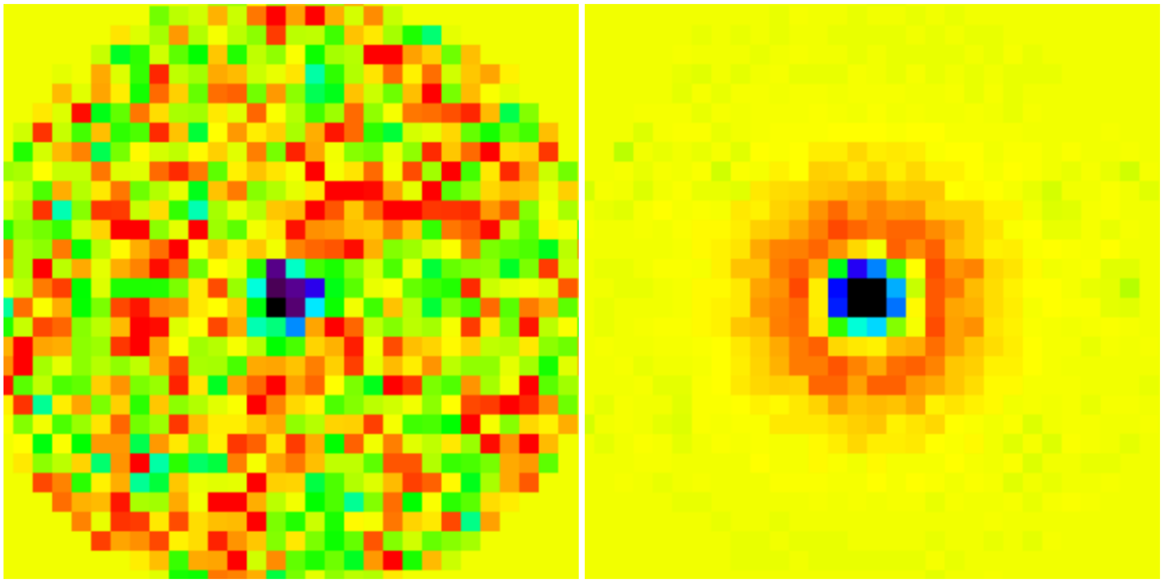

FIG. 7.— *Left* – Average SZ profile map obtained from stacking the *WMAP* 7-year filtered W-band data at the locations of the 175 SZ clusters in the *Planck* ESZ catalogue. The color scale ranges from –4 mK (black) to +1 mK (red). *Right* – The corresponding prediction based on stacking the universal pressure profile scaled by the *Planck*-measured Comptonization parameter, Y_{500}. The "Mexican-hat" like ring is the results of applying matched filter.

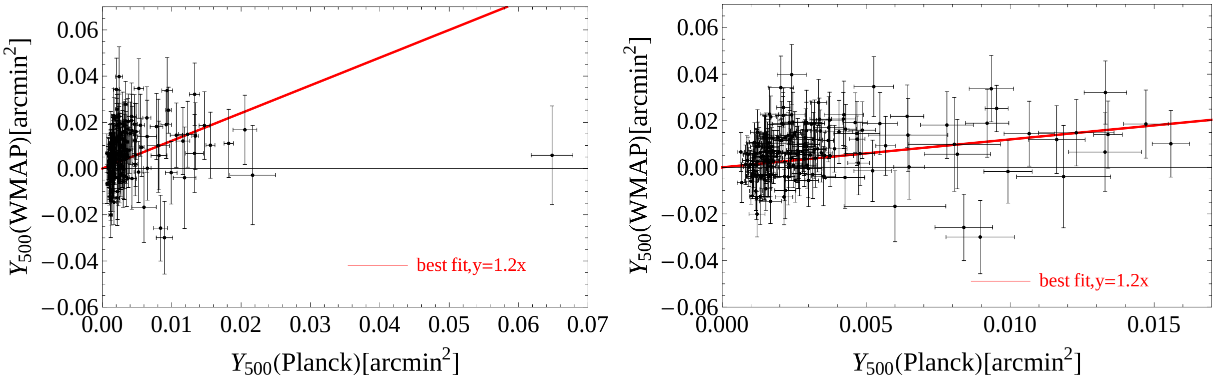

FIG. 8.— Comparison of 175 individual SZ cluster measurements, Y_{500}, from *WMAP* and *Planck*. The left panel shows the comparison full scale, the right panel zooms to a smaller Y_{500} range. We use the relation $Y_{500} \simeq Y_{5R500}/1.8$ to obtain Y_{500} from the *Planck* catalog.

Next we compare of $Y_{500}^{\rm wmap}$ and $Y_{500}^{\rm planck}$ for each cluster. In a linear regression analysis that accounts for errors in both measurements, we find the best-fit slope is 1.23 ± 0.18, which is consistent with unity at the 2σ confidence level. We further consider some systematic error sources that could lead to a slope slightly greater than unity. Our results show that there is no fundamental problems with reliability of the ESZ or calibration of the SZ amplitude. Similar conclusion was also drawn from 3rd version of Whitbourn, Shanks & Sawangwit (2011).

The filtering technique presented here could easily be extended to other surveys, such as ACT and SPT. We plan to revisit this issue when the appropriate data are publicly available.

ACKNOWLEDGMENTS

The authors acknowledge the use of the Healpix package and the LAMBDA Data Center (http://lambda.gsfc.nasa.gov/). We thank Kris Sigurdson and Jim Zibin for helpful discussions. This research was supported by the Natural Sciences and Engineering Research Council of Canada. Y.Z.M is supported by a CITA National Fellowship. G.H. is supported, in part, by the Canadian Institute for Advanced Research.

APPENDIX

LIKELIHOOD FUNCTION FOR DATA WITH BOTH X AND Y ERRORS

In the comparison of $Y^{\rm WMAP}$ and $Y^{\rm Planck}$, we would like to apply a linear regression model for these two quantities. Since both directions have their errors, we need to consider two-dimensional errors when fitting of the slope parameter (see also Clutton-Brock 1967).

Suppose we have one data point (x, y), as plotted in Fig. 9, with measurement errors in both directions $(\delta x, \delta y)$. The function we want to fit is $Y = f(X)$, then (X, Y) can be any point on the curve. In practise, (X, Y) should be fairly close to the data point

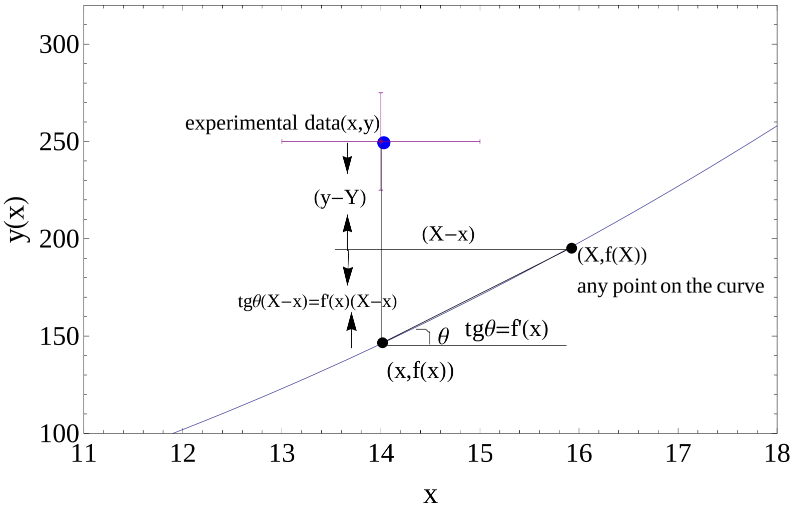

FIG. 9.— Geometric relation between any point on a given function $(X, f(X))$, and experimental data point (x, y) with error $(\delta x, \delta y)$.

(x, y). We want to measure

$$\begin{aligned} y - f(x) &= (y - Y) + (Y - f(x)) \\ &= (y - Y) + (f(X) - f(x)) \\ &= (y - Y) + \tan\theta(X - x) \\ &= (y - Y) + f'(x)(X - x). \end{aligned} \tag{A1}$$

The geometric relationship between these quantities have been illustrated in Fig. 9. Therefore,

$$\begin{aligned} \mathrm{Var(y - f(x))} &= \mathrm{Var(y - Y)} + \mathrm{f'(x)^2 Var((X - x))} \\ &= \delta y^2 + f'(x)^2 \delta x^2. \end{aligned} \tag{A2}$$

Therefore, for just one data, we have the likelihood for the function $f(x)$ as

$$\mathcal{L}(f(x)) = \frac{1}{\left[2\pi\left(\delta y^2 + f'(x)^2 \delta x^2\right)\right]^{\frac{1}{2}}} \exp\left[-\frac{1}{2}\left(\frac{(y - f(x))^2}{\left(\delta y^2 + f'(x)^2 \delta x^2\right)}\right)\right]. \tag{A3}$$

We generalize above equation for a data set with N independent data $(x_k, y_k, \delta x_k, \delta y_k)$, then we have

$$\mathcal{L}(f(x)) = \prod_{k=1}^{N} \frac{1}{\left[2\pi\left(\delta y_k^2 + f'(x_k)^2 \delta x_k^2\right)\right]^{\frac{1}{2}}} \exp\left[-\frac{1}{2}\left(\frac{(y_k - f(x_k))^2}{\left(\delta y_k^2 + f'(x_k)^2 \delta x_k^2\right)}\right)\right]. \tag{A4}$$

Therefore, for the case of a linear regression model $y = a * x$, the likelihood for parameter a becomes

$$\mathcal{L}(a) = \prod_{k=1}^{N} \frac{1}{\left[2\pi\left(\delta y_k^2 + (a\delta x_k)^2\right)\right]^{\frac{1}{2}}} \exp\left[-\frac{1}{2}\left(\frac{(y_k - a * x_k)^2}{\left(\delta y_k^2 + (a\delta x_k)^2\right)}\right)\right]. \tag{A5}$$

REFERENCES

Aghanim N., de Luca A., Bouchet F. R., Gispert R., & Puget J. L., 1997, A&A, 325, 9
Arnaud M. et al., 2010, A&A, 517, 92
Birkinshaw M., & Gull S. F., 1978, Nature, 274, 111
Birkinshaw M., 1999, Phys. Rep., 310, 97
Carlstrom J. E., Holder G. P., & Reese E. D., 2002, ARA&A, 40, 643
Carlstrom J. E., 2011, Publ. Astron. Soc. Pac. 123, 568-581
Clutton-Brock M., 1967, Technometrics, 9, 261
Douspis M., Aghanim N., & Langer M., 2006, A&A, 456, 819
Haiman Z., Mohr J. J., & Holder G. P., 2001, ApJ, 553, 545
Hand N., et al., 1203.4219 [arXiv:astro-ph]
Hinshaw G. et al., 2007, ApJS, 170, 288
Komatsu E., 2011, ApJS., 192, 18
WMAP Lambda website: http://lambda.gsfc.nasa.gov/
Levine E. S., Schulz A. E., & White M., 2002, ApJ, 577, 569
Majumdar S., & Mohr J. J., 2004, ApJ, 613, 41
Marriage T. A., 2011, ApJ, 737, 61
Melin J., Bartlett J. G., Delabrouille J., 2006, A&A, 459, 341
McCarthy I. G., Bower R. G., Balogh M. L., 2007, MNRAS, 377, 1457-1463
Nagai D., Kravtsov A. V., & Vikhlinin A., 2007, ApJ, 668, 1
Planck ERCSC website: http://www.rssd.esa.int/Planck
The Planck Collaboration, 2005, *The Scientific Programme of Planck*, eds. G. Efstathiou, C. Lawrence, and J. Tauber, ESA-SCI(2005), ESA Publications.
Planck Collaboration VII, 2011, A&A, 536, 7
Planck Collaboration VIII, 2011, A&A, 536, 8
Planck Collaboration IX, 2011, A&A, 536, 9
Planck Collaboration XII, 2011, A&A, 536, 12
Tegmark M. & Efstathiou G., 1996, MNRAS, 281, 1297
Tegmark M. & de Oliveira-Costa A., 1998, ApJ, 500, 83
Shaw L. D., Rudd D. H., & Nagai D., 1109.0553, [arXiv:astro-ph]
Sunyaev R. A., & Zeldovich Y. B., 1972, Comments on Astrophysics and Space Physics, 4, 173
Sunyaev R. A., & Zeldovich I. B., 1980, ARA&A, 18, 537

TABLE 2
WMAP OBSERVATIONS OF *Planck* ESZ CLUSTERS

Index	Gal lon (l) (deg)	Gal lat (b) (deg)	Redshift	θ_{500} (arcmin)	$Y_{500}^{\rm planck}$ (arcmin^2)	$\delta Y_{500}^{\rm planck}$ (arcmin^2)	$Y_{500}^{\rm wmap}$ (arcmin^2)	$\delta Y_{500}^{\rm wmap}$ (arcmin^2)
1	0.4409	–41.8351	0.1651	6.3071	$0.14E-02$	$0.27E-03$	$0.48E-02$	$0.92E-02$
2	2.7497	–56.1827	0.1411	7.1114	$0.17E-02$	$0.27E-03$	$0.71E-02$	$0.10E-01$
3	3.9081	–59.4171	0.1510	7.6784	$0.33E-02$	$0.28E-03$	$0.27E-01$	$0.10E-01$
4	6.4760	50.5490	0.0766	15.5982	$0.99E-02$	$0.84E-03$	$-0.18E-02$	$0.14E-01$
5	6.7046	–35.5407	0.0894	10.5796	$0.32E-02$	$0.44E-03$	$0.39E-02$	$0.13E-01$
6	6.7849	30.4683	0.2030	7.5616	$0.95E-02$	$0.40E-03$	$0.25E-01$	$0.10E-01$
7	8.3005	–64.7564	0.3120	8.7664	$0.27E-02$	$0.56E-03$	$0.63E-02$	$0.11E-01$
8	8.4486	–56.3564	0.1486	6.7883	$0.13E-02$	$0.26E-03$	$-0.44E-02$	$0.97E-02$
9	8.9362	–81.2386	0.3066	4.6335	$0.23E-02$	$0.27E-03$	$0.19E-01$	$0.87E-02$
10	18.5314	–25.7228	0.3171	4.1424	$0.15E-02$	$0.22E-03$	$-0.52E-02$	$0.84E-02$
11	21.0918	33.2560	0.1514	9.0695	$0.42E-02$	$0.41E-03$	$0.20E-01$	$0.11E-01$
12	29.0054	44.5625	0.0353	21.7792	$0.82E-02$	$0.12E-02$	$0.56E-02$	$0.15E-01$
13	33.4614	–48.4318	0.0943	8.8429	$0.30E-02$	$0.34E-03$	$-0.56E-02$	$0.11E-01$
14	33.7814	77.1628	0.0622	17.1573	$0.93E-02$	$0.77E-03$	$0.33E-01$	$0.13E-01$
15	36.7219	14.9232	0.1525	7.0561	$0.19E-02$	$0.34E-03$	$0.58E-02$	$0.98E-02$
16	39.8595	–39.9889	0.1760	5.9780	$0.17E-02$	$0.29E-03$	$0.30E-02$	$0.94E-02$
17	42.8257	56.6172	0.0723	12.6087	$0.55E-02$	$0.61E-03$	$0.18E-01$	$0.13E-01$
18	44.2253	48.6842	0.0894	14.0653	$0.13E-01$	$0.74E-03$	$0.32E-01$	$0.13E-01$
19	46.0815	27.1816	0.3890	3.5573	$0.12E-02$	$0.19E-03$	$0.87E-02$	$0.76E-02$
20	46.5037	–49.4389	0.0846	10.8945	$0.35E-02$	$0.42E-03$	$-0.38E-02$	$0.13E-01$
21	46.8830	56.4988	0.1145	9.0824	$0.37E-02$	$0.46E-03$	$0.20E-01$	$0.11E-01$
22	48.0522	57.1769	0.0777	10.9294	$0.37E-02$	$0.54E-03$	$0.17E-01$	$0.13E-01$
23	49.2044	30.8618	0.1644	7.2635	$0.24E-02$	$0.30E-03$	$0.39E-02$	$0.97E-02$
24	49.3365	44.3823	0.0972	8.5539	$0.30E-02$	$0.48E-03$	$-0.52E-03$	$0.11E-01$
25	49.6670	–49.5094	0.0980	9.5536	$0.21E-02$	$0.37E-03$	$0.18E-01$	$0.12E-01$
26	53.4434	–36.2698	0.3250	1.6148	$0.98E-03$	$0.19E-03$	$0.12E-02$	$0.59E-02$
27	53.5227	59.5442	0.1130	8.8081	$0.31E-02$	$0.43E-03$	$0.53E-02$	$0.11E-01$
28	55.6010	31.8644	0.2240	6.1481	$0.27E-02$	$0.26E-03$	$-0.26E-02$	$0.99E-02$
29	55.9755	–34.8850	0.1244	6.7696	$0.20E-02$	$0.28E-03$	$0.65E-02$	$0.98E-02$
30	56.8121	36.3165	0.0953	10.6714	$0.32E-02$	$0.40E-03$	$0.75E-02$	$0.12E-01$
31	56.9685	–55.0798	0.4470	3.5090	$0.16E-02$	$0.20E-03$	$0.86E-02$	$0.76E-02$
32	57.2694	–45.3577	0.3970	4.3122	$0.18E-02$	$0.21E-03$	$0.68E-02$	$0.86E-02$
33	57.3362	88.0113	0.0231	40.6731	$0.65E-01$	$0.30E-02$	$0.56E-02$	$0.21E-01$
34	57.6138	34.9421	0.0802	10.4783	$0.29E-02$	$0.39E-03$	$0.37E-02$	$0.13E-01$
35	57.9289	27.6442	0.0757	11.7297	$0.20E-02$	$0.43E-03$	$0.34E-01$	$0.13E-01$
36	58.2818	18.5938	0.0650	12.5308	$0.48E-02$	$0.50E-03$	$0.58E-02$	$0.13E-01$
37	62.4239	–46.4150	0.0906	9.4655	$0.23E-02$	$0.39E-03$	$-0.41E-02$	$0.12E-01$
38	62.9261	43.7096	0.0299	27.6348	$0.13E-01$	$0.13E-02$	$0.65E-02$	$0.16E-01$
39	67.2317	67.4641	0.1712	7.4168	$0.31E-02$	$0.30E-03$	$-0.30E-02$	$0.10E-01$
40	71.6149	29.7983	0.1565	5.4367	$0.13E-02$	$0.20E-03$	$0.62E-02$	$0.92E-02$
41	72.6308	41.4639	0.2280	6.2793	$0.47E-02$	$0.27E-03$	$0.12E-01$	$0.97E-02$
42	72.8026	–18.7212	0.1430	7.4432	$0.28E-02$	$0.54E-03$	$0.97E-02$	$0.96E-02$
43	73.9652	–27.8216	0.2329	6.2334	$0.31E-02$	$0.26E-03$	$0.18E-01$	$0.96E-02$
44	77.9099	–26.6467	0.1470	7.2926	$0.22E-02$	$0.30E-03$	$0.12E-01$	$0.10E-01$
45	80.3824	–33.2035	0.1072	7.8795	$0.22E-02$	$0.35E-03$	$-0.39E-02$	$0.97E-02$
46	80.9954	–50.9072	0.2998	4.5969	$0.15E-02$	$0.25E-03$	$0.13E-01$	$0.89E-02$
47	83.2875	–31.0322	0.4120	3.9787	$0.12E-02$	$0.22E-03$	$-0.10E-01$	$0.87E-02$
48	85.9999	26.7107	0.1790	11.3240	$0.24E-02$	$0.10E-02$	$0.12E-01$	$0.12E-01$
49	86.4555	15.2999	0.2600	4.9172	$0.17E-02$	$0.15E-03$	$0.41E-03$	$0.91E-02$
50	92.7308	73.4614	0.2279	5.5586	$0.25E-02$	$0.25E-03$	$0.14E-01$	$0.90E-02$
51	93.9197	34.9077	0.0809	11.6216	$0.57E-02$	$0.34E-03$	$0.91E-02$	$0.13E-01$
52	94.0187	27.4256	0.2990	8.0500	$0.16E-02$	$0.80E-03$	$0.10E-01$	$0.10E-01$
53	96.8523	52.4668	0.3179	4.1455	$0.81E-03$	$0.14E-03$	$0.11E-02$	$0.83E-02$
54	97.7396	38.1199	0.1709	6.3915	$0.24E-02$	$0.17E-03$	$0.13E-01$	$0.96E-02$
55	98.9502	24.8610	0.0928	8.2040	$0.12E-02$	$0.23E-03$	$0.95E-03$	$0.11E-01$
56	106.7311	–83.2257	0.2924	4.2902	$0.20E-02$	$0.24E-03$	$0.11E-01$	$0.83E-02$
57	107.1124	65.3142	0.2799	4.9453	$0.17E-02$	$0.20E-03$	$0.21E-01$	$0.88E-02$
58	110.9809	31.7338	0.0581	16.6276	$0.13E-01$	$0.50E-03$	$0.14E-01$	$0.14E-01$
59	112.4561	57.0378	0.0701	11.2395	$0.29E-02$	$0.35E-03$	$0.15E-01$	$0.13E-01$
60	113.8229	44.3503	0.2250	4.6399	$0.65E-03$	$0.13E-03$	$0.65E-02$	$0.87E-02$

TABLE 3
WMAP OBSERVATIONS OF *Planck* ESZ CLUSTERS

Index	Gal lon (l) (deg)	Gal lat (b) (deg)	Redshift	θ_{500} (arcmin)	$Y_{500}^{\rm planck}$ (arcmin^2)	$\delta Y_{500}^{\rm planck}$ (arcmin^2)	$Y_{500}^{\rm wmap}$ (arcmin^2)	$\delta Y_{500}^{\rm wmap}$ (arcmin^2)
61	114.3368	64.8740	0.2836	4.1782	0.11$E-02$	0.18$E-03$	0.11$E-01$	0.85$E-02$
62	115.1624	−72.0911	0.0555	18.8448	0.12$E-01$	0.99$E-03$	0.12$E-01$	0.15$E-01$
63	118.4482	39.3351	0.3967	3.4480	0.86$E-03$	0.14$E-03$	0.58$E-02$	0.74$E-02$
64	118.6016	28.5586	0.1780	5.9658	0.12$E-02$	0.25$E-03$	0.15$E-01$	0.96$E-02$
65	124.2179	−36.4859	0.1971	6.2310	0.28$E-02$	0.38$E-03$	0.66$E-02$	0.96$E-02$
66	125.5865	−64.1447	0.0442	17.7296	0.78$E-02$	0.92$E-03$	0.18$E-01$	0.14$E-01$
67	125.7057	53.8566	0.3019	4.1887	0.10$E-02$	0.15$E-03$	−0.38$E-02$	0.87$E-02$
68	139.1979	56.3560	0.3220	3.7032	0.68$E-03$	0.16$E-03$	−0.65$E-02$	0.79$E-02$
69	143.2459	65.2152	0.2110	4.8535	0.12$E-02$	0.19$E-03$	0.10$E-01$	0.90$E-02$
70	146.3311	−15.5913	0.0172	39.9005	0.22$E-01$	0.33$E-02$	−0.28$E-02$	0.21$E-01$
71	149.2421	54.1894	0.1369	7.3566	0.29$E-02$	0.26$E-03$	0.10$E-01$	0.97$E-02$
72	149.7332	34.6991	0.1818	6.9874	0.33$E-02$	0.30$E-03$	0.78$E-02$	0.93$E-02$
73	159.8592	−73.4730	0.2060	5.6338	0.29$E-02$	0.29$E-03$	0.87$E-02$	0.97$E-02$
74	161.4447	26.2337	0.0381	17.7570	0.42$E-02$	0.68$E-03$	0.22$E-01$	0.14$E-01$
75	163.7234	53.5331	0.1580	6.4145	0.17$E-02$	0.23$E-03$	−0.30$E-02$	0.98$E-02$
76	164.1859	−38.8932	0.0739	14.8848	0.11$E-01$	0.87$E-03$	0.14$E-01$	0.13$E-01$
77	165.0876	54.1196	0.1440	7.1812	0.15$E-02$	0.26$E-03$	0.12$E-01$	0.97$E-02$
78	166.1319	43.3926	0.2172	5.6392	0.21$E-02$	0.24$E-03$	0.11$E-01$	0.91$E-02$
79	167.6563	17.6484	0.1740	6.3019	0.25$E-02$	0.30$E-03$	0.89$E-03$	0.92$E-02$
80	171.9474	−40.6552	0.2700	5.9117	0.34$E-02$	0.32$E-03$	0.15$E-01$	0.94$E-02$
81	172.8864	65.3231	0.0794	9.4305	0.16$E-02$	0.33$E-03$	0.23$E-01$	0.11$E-01$
82	176.2823	−35.0506	0.0347	25.2705	0.65$E-02$	0.14$E-02$	0.14$E-01$	0.16$E-01$
83	180.2409	21.0459	0.5460	3.5482	0.15$E-02$	0.21$E-03$	0.13$E-01$	0.77$E-02$
84	180.6237	76.6529	0.2138	5.0805	0.15$E-02$	0.21$E-03$	−0.91$E-02$	0.94$E-02$
85	182.4440	−28.2986	0.0882	13.0626	0.92$E-02$	0.75$E-03$	0.19$E-01$	0.13$E-01$
86	182.6361	55.8245	0.2060	5.4790	0.11$E-02$	0.23$E-03$	−0.38$E-02$	0.91$E-02$
87	186.3949	37.2555	0.2820	5.0003	0.28$E-02$	0.25$E-03$	0.53$E-02$	0.86$E-02$
88	195.6242	44.0521	0.2952	3.8369	0.92$E-03$	0.19$E-03$	0.11$E-03$	0.80$E-02$
89	195.7735	−24.3063	0.2030	6.2071	0.25$E-02$	0.34$E-03$	−0.55$E-02$	0.92$E-02$
90	205.9614	−39.4838	0.4430	4.0854	0.21$E-02$	0.23$E-03$	0.25$E-01$	0.85$E-02$
91	209.5639	−36.4936	0.0326	25.2364	0.90$E-02$	0.12$E-02$	−0.29$E-01$	0.15$E-01$
92	216.6243	47.0225	0.3826	3.9972	0.12$E-02$	0.20$E-03$	0.59$E-02$	0.83$E-02$
93	218.8563	35.5065	0.1751	6.3049	0.15$E-02$	0.28$E-03$	0.13$E-01$	0.94$E-02$
94	226.1795	−21.9123	0.0989	9.1053	0.26$E-02$	0.39$E-03$	0.55$E-02$	0.11$E-01$
95	226.2475	76.7657	0.1427	7.9934	0.32$E-02$	0.35$E-03$	0.19$E-01$	0.10$E-01$
96	228.1552	75.1923	0.5450	3.1858	0.88$E-03$	0.18$E-03$	0.29$E-02$	0.78$E-02$
97	228.4974	53.1289	0.1434	6.7173	0.12$E-02$	0.28$E-03$	−0.20$E-01$	0.96$E-02$
98	229.2177	−17.2471	0.1710	5.6620	0.17$E-02$	0.26$E-03$	0.87$E-02$	0.93$E-02$
99	229.6413	77.9642	0.2690	4.2806	0.15$E-02$	0.23$E-03$	−0.54$E-02$	0.83$E-02$
100	229.9437	15.2954	0.0704	13.4113	0.64$E-02$	0.58$E-03$	0.22$E-01$	0.13$E-01$
101	234.5921	73.0189	0.0214	33.9178	0.81$E-02$	0.16$E-02$	0.97$E-02$	0.19$E-01$
102	236.9552	−26.6707	0.1483	7.1602	0.17$E-02$	0.29$E-03$	0.83$E-02$	0.10$E-01$
103	239.2841	24.7690	0.0542	18.1124	0.18$E-01$	0.68$E-03$	0.11$E-01$	0.15$E-01$
104	239.2893	−25.9962	0.4070	3.4432	0.14$E-02$	0.32$E-03$	0.46$E-02$	0.74$E-02$
105	241.7429	−30.8853	0.2708	4.4853	0.16$E-02$	0.20$E-03$	0.65$E-02$	0.85$E-02$
106	241.7782	−24.0010	0.1392	7.5582	0.21$E-02$	0.28$E-03$	0.22$E-01$	0.10$E-01$
107	241.8563	51.5311	0.0700	9.7408	0.13$E-02$	0.37$E-03$	−0.12$E-01$	0.12$E-01$
108	241.9745	14.8562	0.1687	6.2748	0.23$E-02$	0.26$E-03$	0.13$E-01$	0.94$E-02$
109	243.5701	67.7603	0.0834	10.4394	0.34$E-02$	0.40$E-03$	0.61$E-02$	0.12$E-01$
110	244.3430	−32.1379	0.2839	4.9752	0.16$E-02$	0.21$E-03$	0.22$E-02$	0.87$E-02$
111	244.6968	32.4925	0.1535	6.2505	0.16$E-02$	0.25$E-03$	−0.32$E-02$	0.93$E-02$
112	246.5206	−26.0574	0.0468	15.4600	0.29$E-02$	0.54$E-03$	0.19$E-01$	0.14$E-01$
113	247.1750	−23.3277	0.1520	6.3719	0.11$E-02$	0.23$E-03$	−0.37$E-02$	0.11$E-01$
114	249.8766	−39.8654	0.1501	6.2807	0.10$E-02$	0.22$E-03$	−0.58$E-02$	0.96$E-02$
115	250.9065	−36.2550	0.2000	5.5837	0.16$E-02$	0.21$E-03$	0.10$E-01$	0.92$E-02$
116	252.9668	−56.0549	0.0752	13.1950	0.26$E-02$	0.39$E-03$	0.71$E-02$	0.13$E-01$
117	253.4796	−33.7242	0.1913	5.3897	0.12$E-02$	0.19$E-03$	−0.13$E-01$	0.94$E-02$
118	256.4510	−65.7122	0.2195	5.3944	0.16$E-02$	0.22$E-03$	0.33$E-02$	0.94$E-02$
119	257.3436	−22.1833	0.2026	5.1414	0.11$E-02$	0.16$E-03$	−0.24$E-02$	0.88$E-02$
120	260.0328	−63.4448	0.2836	4.6171	0.13$E-02$	0.19$E-03$	0.43$E-02$	0.87$E-02$

TABLE 4
WMAP OBSERVATIONS OF *Planck* ESZ CLUSTERS

Index	Gal lon (l) (deg)	Gal lat (b) (deg)	Redshift	θ_{500} (arcmin)	$Y_{500}^{\rm planck}$ (arcmin^2)	$\delta Y_{500}^{\rm planck}$ (arcmin^2)	$Y_{500}^{\rm wmap}$ (arcmin^2)	$\delta Y_{500}^{\rm wmap}$ (arcmin^2)
121	262.2535	−35.3691	0.2952	4.8608	0.19*E*−02	0.14*E*−03	0.46*E*−02	0.88*E*−02
122	262.7108	−40.9137	0.3900	3.7414	0.11*E*−02	0.13*E*−03	−0.31*E*−02	0.79*E*−02
123	263.1612	−23.4141	0.2266	5.7940	0.18*E*−02	0.18*E*−03	0.27*E*−02	0.93*E*−02
124	263.2091	−25.2105	0.0506	15.3956	0.41*E*−02	0.48*E*−03	0.15*E*−01	0.14*E*−01
125	263.6653	−22.5362	0.1644	7.1784	0.36*E*−02	0.22*E*−03	0.51*E*−02	0.99*E*−02
126	265.0068	−48.9483	0.0590	15.5042	0.65*E*−02	0.53*E*−03	0.15*E*−03	0.13*E*−01
127	266.0384	−21.2523	0.2965	5.3920	0.37*E*−02	0.18*E*−03	0.11*E*−01	0.92*E*−02
128	266.8423	25.0788	0.2542	5.4913	0.15*E*−02	0.23*E*−03	0.27*E*−02	0.90*E*−02
129	269.3112	−49.8784	0.0853	9.4591	0.22*E*−02	0.36*E*−03	−0.98*E*−02	0.12*E*−01
130	269.5163	26.4247	0.0126	43.3013	0.12*E*−01	0.16*E*−02	−0.39*E*−02	0.22*E*−01
131	271.1969	−30.9695	0.3700	4.0128	0.11*E*−02	0.12*E*−03	0.10*E*−02	0.80*E*−02
132	271.5017	−56.5590	0.3000	4.0513	0.14*E*−02	0.39*E*−03	−0.35*E*−02	0.82*E*−02
133	272.1077	−40.1502	0.0589	16.8371	0.16*E*−01	0.65*E*−03	0.10*E*−01	0.14*E*−01
134	273.6439	63.2815	0.1339	7.5915	0.28*E*−02	0.40*E*−03	0.88*E*−02	0.10*E*−01
135	275.2199	43.9212	0.1068	8.6906	0.24*E*−02	0.46*E*−03	0.22*E*−01	0.11*E*−01
136	277.7522	−51.7307	0.4400	3.5019	0.15*E*−02	0.18*E*−03	0.14*E*−01	0.77*E*−02
137	278.6061	39.1716	0.3075	4.6768	0.19*E*−02	0.30*E*−03	0.13*E*−01	0.86*E*−02
138	280.1968	47.8167	0.1557	6.1951	0.23*E*−02	0.34*E*−03	−0.17*E*−04	0.99*E*−02
139	282.4933	65.1743	0.0766	12.0485	0.53*E*−02	0.69*E*−03	0.34*E*−01	0.13*E*−01
140	284.4608	52.4371	0.4414	3.6666	0.16*E*−02	0.25*E*−03	0.47*E*−02	0.78*E*−02
141	284.9936	−23.7081	0.3900	3.9007	0.13*E*−02	0.12*E*−03	0.89*E*−02	0.81*E*−02
142	285.6352	−17.2466	0.3500	3.5369	0.90*E*−03	0.15*E*−03	0.53*E*−02	0.77*E*−02
143	286.5869	−31.2510	0.2100	5.6231	0.14*E*−02	0.21*E*−03	−0.34*E*−02	0.91*E*−02
144	286.9927	32.9157	0.3900	5.0661	0.34*E*−02	0.33*E*−03	0.20*E*−01	0.91*E*−02
145	288.6160	−37.6562	0.1270	7.1712	0.29*E*−02	0.31*E*−03	0.90*E*−03	0.98*E*−02
146	292.5194	21.9886	0.3000	5.1319	0.21*E*−02	0.34*E*−03	0.18*E*−01	0.91*E*−02
147	294.6674	−37.0299	0.2742	4.4588	0.15*E*−02	0.20*E*−03	0.68*E*−02	0.84*E*−02
148	295.3328	23.3359	0.1190	7.2625	0.23*E*−02	0.43*E*−03	0.15*E*−02	0.10*E*−01
149	296.4139	−32.4851	0.0613	12.4130	0.25*E*−02	0.40*E*−03	0.19*E*−01	0.13*E*−01
150	303.7589	33.6561	0.0544	13.6334	0.47*E*−02	0.80*E*−03	0.14*E*−01	0.13*E*−01
151	304.4970	32.4428	0.0554	13.9820	0.37*E*−02	0.82*E*−03	0.49*E*−02	0.13*E*−01
152	304.6716	−31.6688	0.1934	5.1350	0.11*E*−02	0.20*E*−03	−0.14*E*−02	0.89*E*−02
153	304.8952	45.4509	0.0473	17.6562	0.84*E*−02	0.10*E*−02	−0.25*E*−01	0.14*E*−01
154	306.6839	61.0626	0.0845	11.5603	0.52*E*−02	0.65*E*−03	−0.15*E*−02	0.12*E*−01
155	306.8008	58.6075	0.0845	11.8327	0.43*E*−02	0.68*E*−03	−0.43*E*−02	0.13*E*−01
156	311.9973	30.7170	0.0480	19.4676	0.12*E*−01	0.13*E*−02	0.15*E*−01	0.14*E*−01
157	313.3604	61.1166	0.1832	7.4682	0.39*E*−02	0.44*E*−03	0.78*E*−02	0.95*E*−02
158	313.8723	−17.1066	0.1530	8.1257	0.43*E*−02	0.38*E*−03	0.16*E*−01	0.11*E*−01
159	315.7076	−18.0430	0.1050	9.6202	0.49*E*−02	0.46*E*−03	0.16*E*−01	0.11*E*−01
160	316.3467	28.5433	0.0391	24.8271	0.21*E*−01	0.17*E*−02	0.17*E*−01	0.16*E*−01
161	318.1334	−29.5778	0.2170	5.1100	0.17*E*−02	0.26*E*−03	0.31*E*−02	0.86*E*−02
162	321.9628	−47.9754	0.0940	9.9841	0.29*E*−02	0.32*E*−03	0.13*E*−01	0.12*E*−01
163	324.4983	−44.9709	0.0951	8.9942	0.21*E*−02	0.30*E*−03	−0.13*E*−01	0.11*E*−01
164	332.2345	−46.3695	0.0980	10.4829	0.47*E*−02	0.38*E*−03	0.18*E*−02	0.12*E*−01
165	332.8879	−19.2803	0.1470	7.1985	0.24*E*−02	0.32*E*−03	0.59*E*−02	0.97*E*−02
166	335.5923	−46.4637	0.0760	11.4352	0.46*E*−02	0.42*E*−03	0.19*E*−01	0.13*E*−01
167	336.5914	−55.4487	0.0965	9.5308	0.32*E*−02	0.32*E*−03	0.12*E*−01	0.12*E*−01
168	340.8860	−33.3489	0.0556	18.6213	0.15*E*−01	0.78*E*−03	0.18*E*−01	0.15*E*−01
169	340.9585	35.1160	0.2357	6.0862	0.17*E*−02	0.38*E*−03	−0.14*E*−01	0.98*E*−02
170	342.3172	−34.9065	0.2320	4.8257	0.16*E*−02	0.24*E*−03	−0.41*E*−02	0.91*E*−02
171	342.8155	−30.4605	0.0600	10.9597	0.24*E*−02	0.51*E*−03	0.39*E*−01	0.13*E*−01
172	345.4068	−39.3440	0.0448	23.7182	0.60*E*−02	0.18*E*−02	−0.16*E*−01	0.15*E*−01
173	346.5981	35.0477	0.2226	5.3936	0.26*E*−02	0.31*E*−03	0.31*E*−03	0.89*E*−02
174	347.1876	−27.3538	0.2371	4.9553	0.12*E*−02	0.24*E*−03	0.25*E*−02	0.93*E*−02
175	349.4626	−59.9475	0.3475	4.9888	0.25*E*−02	0.19*E*−03	0.15*E*−01	0.92*E*−02

Weller J., Battye R. A., & Kneissl R., 2002, Phys. Rev. Lett., 88, 231301
Whitbourn J. R., Shanks T., & Sawangwit U., arXiv:1107.2654 [astro-ph].
Zwart J. T. L. et al., 2008, MNRAS, 391, 1545